Supporting Information for "`LoadDef`: A Python-based toolkit to model elastic deformation caused by surface mass loading on spherically symmetric bodies"

Hilary R. Martens[1*], Luis Rivera[2], and Mark Simons[3]

[1]Department of Geosciences, University of Montana, Missoula, Montana, USA.
[2]Institut de Physique du Globe de Strasbourg, UMR 7516 CNRS, Université de Strasbourg, Strasbourg, France.
[3]Seismological Laboratory, Division of Geological and Planetary Sciences, California Institute of Technology, Pasadena, California, USA.

Contents

Text S1: Software Source Code

The `LoadDef` user manual and source code are distributed under the GNU General Public License v3.0, and are available from `https://github.com/hrmartens/LoadDef`.

Text S2: Equations of Motion

The equations of motion for spheroidal deformation may be written as a system of six first-order differential equations (e.g. Alterman et al., 1959):

$$
\begin{aligned}
\dot{y}_1 &= \frac{-2\lambda}{\lambda+2\mu}\frac{y_1}{r} + \frac{y_2}{\lambda+2\mu} + \frac{\lambda\, n(n+1)}{\lambda+2\mu}\frac{y_3}{r}, \\
\dot{y}_2 &= \left[-\omega^2\rho r^2 - 4\rho g r + \frac{4\mu(3\lambda+2\mu)}{\lambda+2\mu}\right]\frac{y_1}{r^2} - \frac{4\mu}{\lambda+2\mu}\frac{y_2}{r} \\
&+ \left[n(n+1)\rho g r - \frac{2\mu(3\lambda+2\mu)\, n(n+1)}{\lambda+2\mu}\right]\frac{y_3}{r^2} \\
&+ n(n+1)\frac{y_4}{r} - \rho y_6, \\
\dot{y}_3 &= -\frac{y_1}{r} + \frac{y_3}{r} + \frac{y_4}{\mu}, \\
\dot{y}_4 &= \left[g\rho r - \frac{2\mu(3\lambda+2\mu)}{\lambda+2\mu}\right]\frac{y_1}{r^2} - \frac{\lambda}{\lambda+2\mu}\frac{y_2}{r} \\
&+ \left[-\omega^2\rho r^2 + \frac{2\mu}{\lambda+2\mu}[\lambda(2n^2+2n-1) + 2\mu(n^2+n-1)]\right]\frac{y_3}{r^2} \\
&- \frac{3y_4}{r} - \rho\frac{y_5}{r}, \\
\dot{y}_5 &= 4\pi G\rho y_1 + y_6, \\
\dot{y}_6 &= -4\pi G\rho\, n(n+1)\frac{y_3}{r} + n(n+1)\frac{y_5}{r^2} - \frac{2y_6}{r},
\end{aligned}
\tag{1}
$$

where λ and μ are Lamé's parameters, G is the universal gravitational constant, ρ is density, g is gravitational acceleration, n is spherical harmonic degree, r is radius, ω

*32 Campus Dr., Dept. of Geosciences, University of Montana, Missoula, Montana, 59812-1296, USA

Corresponding author: H.R. Martens, `hilary.martens@umontana.edu`

is the angular frequency of oscillation, and dots represent differentiation with respect to r. The variables y_1 and y_3 characterize the radial and tangential displacements, respectively; y_2 and y_4 characterize the radial and tangential stress, respectively; y_5 characterizes the gravitational potential; and the equation for $\dot{y}_5$ defines y_6. We have retained the inertial terms in the equations of motion, which gives rise to the terms that include ω. A summary of surface boundary conditions and Love-number definitions is provided in Table 1 of Martens et al. (2016b).

Text S3: Details on Computing the Load Green's Functions

To improve convergence of the infinite sums involved in computing the load Green's functions (LGFs), we apply Kummer's transformation to each series using second-order asymptotic expressions for the load Love numbers (Farrell, 1972; Guo et al., 2004). The general form of Kummer's transformation is given by (e.g., Abramowitz & Stegun, 1964; Na & Baek, 2011):

$$\sum_n f(n)Q_n = f_\infty \sum_n Q_n + \sum_n (f(n) - f_\infty)\, Q_n, \tag{2}$$

where $f_\infty = \lim_{n\to\infty} f(n)$. Applied to each type of Green's function, we have:

Vertical Displacement:

$$\begin{aligned} u(\theta) \;=\; & \frac{a}{M}\, h_\infty^* \sum_{n=0}^{\infty} P_n(\cos\theta) + \frac{a}{M}\, h_\infty^{**} \sum_{n=1}^{\infty} \frac{1}{n}\, P_n(\cos\theta) + \\ & \frac{a}{M}\,(h_0' - h_\infty^*) + \frac{a}{M} \sum_{n=1}^{N_{\max}} (h_n' - (h_\infty^* + \frac{1}{n}\, h_\infty^{**}))\, P_n(\cos\theta). \end{aligned} \tag{3}$$

Horizontal Displacement:

$$\begin{aligned} v(\theta) \;=\; & \frac{a}{M}\, l_\infty^* \sum_{n=1}^{\infty} \frac{1}{n} \frac{\partial P_n(\cos\theta)}{\partial\theta} + \frac{a}{M}\, l_\infty^{**} \sum_{n=1}^{\infty} \frac{1}{n^2} \frac{\partial P_n(\cos\theta)}{\partial\theta} + \\ & \frac{a}{M} \sum_{n=1}^{N_{\max}} (n l_n' - (l_\infty^* + \frac{1}{n}\, l_\infty^{**}))\, \frac{1}{n} \frac{\partial P_n(\cos\theta)}{\partial\theta}. \end{aligned} \tag{4}$$

Gravity (elastic):

$$g^E = 2g_a \left(\frac{u}{a}\right) - \left(\frac{g_a}{M} \sum_{n=0}^{\infty} \left[n\, k_n'\, P_n(\cos\theta) + n\, k_n' \frac{1}{n}\, P_n(\cos\theta) \right] \right), \tag{5}$$

where

$$\begin{aligned} \sum_{n=0}^{\infty} (n\, k_n')\, P_n(\cos\theta) \;=\; & k_\infty^* \sum_{n=0}^{\infty} P_n(\cos\theta) + k_\infty^{**} \sum_{n=0}^{\infty} \frac{1}{n} P_n(\cos\theta) \\ & + \sum_{n=0}^{N_{\max}} \left[(n(n\, k_n' - k_\infty^*) - k_\infty^{**})/n \right]\, P_n(\cos\theta) \end{aligned} \tag{6}$$

and

$$\sum_{n=0}^{\infty} (n\, k_n') \frac{1}{n}\, P_n(\cos\theta) = k_\infty^* \sum_{n=0}^{\infty} \frac{1}{n}\, P_n(\cos\theta) + \sum_{n=0}^{N_{\max}} (n\, k_n' - k_\infty^*)\, \frac{1}{n}\, P_n(\cos\theta). \tag{7}$$

Tilt (elastic):

$$t^E = \left[\frac{1}{M} \sum_{n=1}^{\infty} h_n' \frac{d}{d\theta} P_n(\cos\theta) \right] - \left[\frac{1}{M} \sum_{n=1}^{\infty} (n k_n') \frac{1}{n} \frac{d}{d\theta} P_n(\cos\theta) \right], \tag{8}$$

where

$$\sum_{n=1}^{\infty} h'_n \frac{d}{d\theta} P_n(\cos\theta) = h^*_\infty \sum_{n=1}^{\infty} \frac{d}{d\theta} P_n(\cos\theta) + h^{**}_\infty \sum_{n=1}^{\infty} \frac{1}{n} \frac{d}{d\theta} P_n(\cos\theta) + \sum_{n=1}^{N_{\max}} \left[(n(h'_n - h^*_\infty) - h^{**}_\infty)/n \right] \frac{d}{d\theta} P_n(\cos\theta) \quad (9)$$

and

$$\sum_{n=1}^{\infty} (n\, k'_n) \frac{1}{n} \frac{d}{d\theta} P_n(\cos\theta) = k^*_\infty \sum_{n=1}^{\infty} \frac{1}{n} \frac{d}{d\theta} P_n(\cos\theta) + k^{**}_\infty \sum_{n=1}^{\infty} \frac{1}{n^2} \frac{d}{d\theta} P_n(\cos\theta) + \sum_{n=1}^{N_{\max}} \left[(n(nk'_n - k^*_\infty) - k^{**}_\infty)/n \right] \frac{1}{n} \frac{d}{d\theta} P_n(\cos\theta). \quad (10)$$

Strain in direction of load ($\epsilon_{\theta\theta}$):

$$\epsilon_{\theta\theta} = \frac{u}{a} + \frac{1}{M} \sum_{n=1}^{\infty} l'_n \frac{d^2}{d\theta^2} P_n(\cos\theta) = \frac{u}{a} + \frac{1}{M} \sum_{n=1}^{\infty} (nl'_n) \frac{1}{n} \frac{d^2}{d\theta^2} P_n(\cos\theta), \quad (11)$$

where

$$\sum_{n=1}^{\infty} (nl'_n) \frac{1}{n} \frac{d^2}{d\theta^2} P_n(\cos\theta) = l^*_\infty \sum_{n=1}^{\infty} \frac{1}{n} \frac{d^2}{d\theta^2} P_n(\cos\theta) + l^{**}_\infty \sum_{n=1}^{\infty} \frac{1}{n^2} \frac{d^2}{d\theta^2} P_n(\cos\theta) + \sum_{n=1}^{N_{\max}} \left[(n(nl'_n - l^*_\infty) - l^{**}_\infty)/n \right] \frac{1}{n} \frac{d^2}{d\theta^2} P_n(\cos\theta). \quad (12)$$

Strain perpendicular to load ($\epsilon_{\lambda\lambda}$):

$$\epsilon_{\lambda\lambda} = \frac{1}{a}\, u + \frac{\cot\theta}{a}\, v. \quad (13)$$

Strain in radial direction (ϵ_{rr}):

$$\epsilon_{rr} = -\frac{\lambda_a}{\lambda_a + 2\mu_a} (\epsilon_{\theta\theta} + \epsilon_{\lambda\lambda}). \quad (14)$$

In the equations above, a is the radius of the planet, M is the mass of the planet, g_a is the surface gravity, λ and μ are Lamé's parameters, λ_a and μ_a are Lamé's parameters at the surface, n is spherical harmonic degree, $N_{\max}$ is the maximum spherical harmonic degree for which Love numbers are computed explicity and beyond which asymptotic values are assumed, h'_n is the vertical-displacement load Love number, l'_n is the horizontal-displacement load Love number, k'_n is the gravitational load Love number, the P_n are the Legendre polynomials, θ is the angular distance from the load point, a subscript infinity (∞) represents an asymptotic load Love number, a single asterisk denotes a first-order asymptotic load Love number, and a double asterisk denotes a second-order asymptotic load Love number.

The second-order asymptotic expansions of the load Love numbers are given by:

$$\begin{aligned} \lim_{n\to\infty} h'_n &\approx h^*_\infty + \frac{1}{n}\, h^{**}_\infty \\ \lim_{n\to\infty} nl'_n &\approx l^*_\infty + \frac{1}{n}\, l^{**}_\infty \\ \lim_{n\to\infty} nk'_n &\approx k^*_\infty + \frac{1}{n}\, k^{**}_\infty, \end{aligned} \quad (15)$$

where a single asterisk represents a first-order asymptotic solution and a double asterisk represents a second-order asymptotic solution.

We also taper the series summands at high spherical-harmonic degrees by computing coefficients that simulate the recursive averaging described in Guo et al. (2004). The taper serves to reduce the amplitudes of series oscillations as n approaches $N_{\max}$, where $N_{\max}$ marks the transition to using asymptotic load Love numbers. The taper consists of a vector of coefficients, with most values equal to one and coefficients being reduced toward zero as n approaches $N_{\max}$ (J.-Y. Guo, personal communication, 2016). The point at which the taper begins depends on the number of iterations desired for the recursive averaging. Taper coefficients are determined by averaging pairs of coefficients from the previous iteration.

`LoadDef` optionally permits the inclusion of a disk factor when computing LGFs. Particularly for the tilt and strain LGFs, inclusion of a disk factor may be necessary to facilitate convergence of the LGFs (Farrell, 1972). A disk factor approximates the point-load as being distributed over a disk of finite size, and provides a reasonable approximation of the point-load source so long as the radius of the disk is much smaller than the angular distance to the load. Formally, the disk factor is given by

$$\left[-\frac{(1+\cos\alpha)}{n(n+1)\sin\alpha}\frac{\partial P_n(\cos\alpha)}{\partial\alpha}\right], \tag{16}$$

where n is the spherical-harmonic degree, α is the angular radius of the circular disk, and P_n represents a Legendre polynomial. The disk factor is valid in the limit $\alpha \to 0$ (e.g., Farrell, 1972). For custom applications, disk-factor settings may be adjusted using keyword arguments, or the disk factor may be removed altogether.

Apparent singularities appear in the horizontal-displacement, tilt, and strain LGFs at the angular-separation distance of 180° (i.e. at the antipode from the load point). We evaluate the necessary limits and sums exactly, which avoids the numerical extrapolations adopted in previous approaches (e.g. Guo et al., 2004).

In the limit $\theta \to 180°$, the Legendre sums reduce to:

$$\lim_{\theta\to 180°}\sum_{n=0}^{\infty} P_n(\cos\theta) = \frac{1}{2} \tag{17}$$

$$\lim_{\theta\to 180°}\sum_{n=0}^{\infty} n\,P_n(\cos\theta) = -\frac{1}{4} \tag{18}$$

$$\lim_{\theta\to 180°}\sum_{n=1}^{\infty} \frac{1}{n}\,P_n(\cos\theta) = -\ln(2) \tag{19}$$

$$\lim_{\theta\to 180°}\sum_{n=1}^{\infty} \frac{\partial P_n(\cos\theta)}{\partial\theta} = 0 \tag{20}$$

$$\lim_{\theta\to 180°}\sum_{n=1}^{\infty} \frac{1}{n}\frac{\partial P_n(\cos\theta)}{\partial\theta} = 0 \tag{21}$$

$$\lim_{\theta\to 180°}\sum_{n=1}^{\infty} \frac{1}{n^2}\frac{\partial P_n(\cos\theta)}{\partial\theta} = 0 \tag{22}$$

$$\lim_{\theta\to 180°}\sum_{n=1}^{\infty} \frac{1}{n}\frac{\partial^2 P_n(\cos\theta)}{\partial\theta^2} = \frac{3}{8} \tag{23}$$

$$\lim_{\theta\to 180°}\sum_{n=1}^{\infty} \frac{1}{n^2}\frac{\partial^2 P_n(\cos\theta)}{\partial\theta^2} = \frac{\ln(2)}{2}+\frac{1}{4}. \tag{24}$$

We evaluated the limits by direct substitution of $\theta = 180°$ into the analytical expressions for the Legendre sums (e.g. Guo et al., 2004) as well as by using the `Python` package `SymPy` (a `Python` library for symbolic computations).

In the limit $\theta \to 180°$, the Legendre functions are given by:

$$\begin{aligned} \lim_{\theta \to 180°} \quad P_n(\cos\theta) &= (-1)^n \\ \lim_{\theta \to 180°} \quad \frac{dP_n(\cos\theta)}{d\theta} &= 0 \\ \lim_{\theta \to 180°} \quad \frac{d^2P_n(\cos\theta)}{d\theta^2} &= (-1)^{n+1}\left(\frac{n\,(n+1)}{2}\right). \end{aligned} \tag{25}$$

For the perpendicular component of strain, $\epsilon_{\lambda\lambda}$ (Eq. 13), a factor of $\cot\theta$ appears in the second term that must also be evaluated in the limit that $\theta \to 180°$. For this component, we evaluate the limit as $\theta \to 180°$ of:

$$\cot(\theta)\,\frac{dP_n(\cos\theta)}{d\theta}, \tag{26}$$

where the Legendre polynomial arises from the series expansion for horizontal displacement, v (Eq. 4). The limit evaluates to:

$$(-1)^{n+1}\left(\frac{n\,(n+1)}{2}\right), \tag{27}$$

which is equivalent to $\lim_{\theta\to 180°}\left(\frac{d^2P_n(\cos\theta)}{d\theta^2}\right)$. Furthermore, the limits of Eqs. 21 and 22 as $\theta \to 180°$ with the $\cot(\theta)$ factor included (see Eqs. 4 and 13) are equivalent to Eqs. 23 and 24, respectively. As a result, $\epsilon_{\lambda\lambda} = \epsilon_{\theta\theta}$ at $\theta = 180°$. This result could also be attained by directly invoking the cylindrical symmetry of the problem.

Text S4: `LoadDef` Performance Tests

We ran `LoadDef` performance tests on a single core of a 2.8 GHz Intel Core i5 processor from a late-2015 iMac (i.e. a standard desktop computer). The test system includes 256 KB of L2 cache per core, 4 MB of L3 cache, and 16 GB of memory. Processing times can be reduced considerably by utilizing `LoadDef`'s MPI processing capabilities and more advanced processors. Below, we provide a snapshot of typical run-times for each of `LoadDef`'s main programs.

run_ln.py (compute Love numbers): 75 minutes to compute 10,001 individual Love numbers from n=0 to n=10,000 for all three classes (potential, load, and shear) and all three types (h, l, and k). Using two cores instead of one cuts the run time approximately in half. Run times also depend on the resolution and radius of the input planetary model, the integration parameters (including tolerances for solution convergence), and the spherical-harmonic degrees computed. Lower degrees take longer to compute than higher degrees because the equations of motion must be integrated starting from deeper within the planet for the lower degrees.

run_pl.py (compute Love number partial derivatives): 32 seconds to compute the three partial derivatives of Love numbers (with respect to density and the two elastic moduli) for spherical harmonic degrees n=0 to n=4 for all three classes (potential, load, and shear) and all three types (h, l, and k) of Love numbers.

run_gf.py (compute Green's functions): 44 seconds to compute vertical displacement, horizontal displacement, gravity, tilt, and strain load Green's functions at 150 angular distances from the load point in three reference frames (CE, CM, CF). Using two cores instead of one cuts the run time approximately in half.

run_cn.py (compute surface displacements): The run time depends significantly on the resolutions of the land-sea mask, integration mesh, and load model. For the default land-sea mask and integration mesh parameters provided with `LoadDef` in its current version, example run times for computing displacements at five geographic locations caused by the M_2 ocean tide include: 2.5 minutes (EOT11a ocean model), 4 minutes (FES2014 ocean model), and 9 minutes (TPXO8-Atlas ocean model). To keep `LoadDef` as general and versatile as possible, the customizable integration mesh is generated on-the-fly during the call to the function. Furthermore, to support a variety of loading applications, the load models are interpolated onto the integration mesh on-the-fly as well. Run times therefore scale significantly with the resolution of the load model. For each station, however, the generation of the integration mesh and interpolation of the land-sea mask only need to be performed once. Thus, repeating the convolution for multiple load models at a single station in a single run is more efficient than performing each convolution at a single station in separate runs.

Data Set S1: Oceanless Variant of PREM

The Earth model is described in Table S1.

Data Set S2: Load Love Numbers for Oceanless PREM

LLNs were computed using the default keyword arguments and integration settings in the current version of `LoadDef`, as described in the User Manual v1.1.1.

Data Set S3: Load Green's Functions for Oceanless PREM | CE frame

LGFs were computed using the default keyword arguments in the current version of `LoadDef`, as described in the User Manual v1.1.1.

Data Set S4: Load Green's Functions for Oceanless PREM | CM frame

Same as Data Set S3, but in the CM frame.

Data Set S5: Load Green's Functions for Oceanless PREM | CF frame

Same as Data Set S3, but in the CF frame.

Data Set S6: Surface Displacements from M_2 ocean tidal loading | CM

Surface displacements (east, north, and up) in the western United States caused by mass loading from the M_2 ocean tide. The FES2014 ocean-tide model and the LGFs from Data Set S4 (oceanless PREM; CM frame) were used to make the computation. We assumed a uniform sea-water density of 1030 kg m^{-3}. We used the `LoadDef`-default land-sea mask based on ETOPO1 and the Antarctic Digital Database, and created the integration meshes using the following settings: $\Delta\theta = 0.0002°$ from $\theta = 0 \rightarrow 0.02°$, $\Delta\theta = 0.001°$ from $\theta = 0.02 \rightarrow 0.05°$, $\Delta\theta = 0.01°$ from $\theta = 0.05 \rightarrow 1.0°$, $\Delta\theta = 0.1°$ from $\theta = 1.0 \rightarrow 10.0°$, $\Delta\theta = 0.5°$ from $\theta = 10.0 \rightarrow 90.0°$, and $\Delta\theta = 1.0°$ from $\theta = 90.0 \rightarrow 180.0°$. We adopted an azimuthal increment of $\alpha = 0.1°$.

Data Set S7: Surface Displacements from O_1 ocean tidal loading | CM

Same as Data Set S6, but for the O_1 tidal harmonic.

Table S1. Original version and oceanless variant of the Preliminary Reference Earth Model

	Original PREM[a]			Oceanless PREM[b]		
Radius (km)	V_P (km/s)	V_S (km/s)	Density (g/cc)	V_P (km/s)	V_S (km/s)	Density (g/cc)
6368-6371	1.450	0.000	1.020	6.18904	3.41464	2.28340
6356-6368	5.800	3.200	2.600	6.18904	3.41464	2.28340
6346.6-6356	6.800	3.900	2.900	6.800	3.900	2.900
6291-6346.6	4.1875	2.1519	2.6910	4.1875	2.1519	2.6910
	$+3.9382x$	$+2.3481x$	$+0.6924x$	$+3.9382x$	$+2.3481x$	$+0.6924x$
6151-6291	4.1875	2.1519	2.6910	4.1875	2.1519	2.6910
	$+3.9382x$	$+2.3481x$	$+0.6924x$	$+3.9382x$	$+2.3481x$	$+0.6924x$

[a]The original version of PREM at a reference period of 1 second from Table 1 of Dziewonski & Anderson (1981). We use the effective isotropic velocities between 24.4–200 km depth. $x = r/a$, where $a = 6371$ km.

[b]The oceanless variant of PREM described in the main text. Following Guo et al. (2004), we compute a weighted-average density for the ocean layer and upper-most crustal layer, ensuring conservation of total mass. The elastic moduli remain equivalent to the upper-most crustal layer.

Data Set S8: Surface Displacements from M_f ocean tidal loading | CM

Same as Data Set S6, but for the M_f tidal harmonic.

Supplementary Table S1

Table S1 lists seismic velocities and densities for the original, isotropic Preliminary Reference Earth Model (PREM) from Table 1 of Dziewonski & Anderson (1981) as well as for the oceanless variant of PREM referred to in the main text. The oceanless variant of PREM is identical to the original PREM with the exception of the outer two layers. In particular, the ocean layer and outer-most crustal layer are combined via a weighted average to conserve total mass (Guo et al., 2004). The elastic moduli remain equivalent to the outer-most crustal layer in the original PREM.

Supplementary Figures

Figure S1 shows partial derivatives of degree-2 load Love numbers for the oceanless variant of PREM described in Table S1.

Displacement LGFs for the oceanless variant of PREM (Table S1) are shown in **Figure S2** for three different reference frames: CE, CM, and CF. Gravity, tilt, and strain LGFs derived from the same Earth model are shown in **Figure S3**.

Figure S4 depicts an example of the template grid used to convolve load Green's functions with a surface mass-load model.

Figure S5 shows a comparison between load Love numbers (LLNs) computed by Guo et al. (2004) and those computed by `LoadDef` for the oceanless variant of PREM. The LLNs included in Table 1 of Guo et al. (2004) reflect a reduced and irregular sampling of the LLNs from $n = 0$ to $n = 10,000$; to remain consistent in the benchmark comparison, we downsample the `LoadDef` results to an equivalent spherical-harmonic degree spacing. **Figures S6-S8** show similar comparisons between `LoadDef`

and LLNs from Farrell (1972), Wang et al. (2012), and Chen et al. (2017). The load Love numbers agree very well in each comparison; it is only by computing the residual differences and reducing the y-axis scales that discrepancies may be discerned.

Figure S9 shows a benchmark comparison between load Green's functions computed by `LoadDef` and those computed by Farrell (1972) for the Gutenberg-Bullen A (GBA) Earth model. The GBA model is tabulated in Table 4 of Alterman et al. (1961). To best match the results of Farrell (1972), it was necessary to characterize the model as a block-type model (i.e. no interpolation between material layers by forcing the top and base of each layer to have the same properties). We also assumed the shear-wave velocities of PREM for the inner core, since shear-wave velocities for the inner core are not included in the GBA model. Inner-core structure affects only the low-degree Love numbers.

Figure S10 shows a benchmark comparison between LGFs computed by `LoadDef` and those computed by Wang et al. (2012) for an oceanless variant of PREM (see supplementary files provided with Wang et al. (2012)). To match the results of Wang et al. (2012), it was necessary to include the Newtonian components of gravity and tilt. We also excluded the degree-0 contribution to the load Green's functions, which Wang et al. (2012) exclude for the purpose of mass conservation.

A comparison between LLN asymptotic expansions of first- and second-order and LLNs computed explicitly by `LoadDef` is shown in **Figure S11**. The second-order asymptotic expansions converge faster to the true load Love numbers than the first-order asymptotic expansions, although the effect diminishes with increasing n.

Figures S12 and S13 depict east and north displacements, respectively, caused by M_2 ocean tidal loading. The predicted surface displacements were computed using `LoadDef`, and compared with an independent software package called `SPOTL` (Agnew, 1997, 2013). Vector differences between the two sets of predictions, computed based on the in-phase and quadrature components of the harmonic responses, are shown in the lower panels of each figure. Discrepancies between the two softwares are small, indicating good agreement. The largest discrepancies are present in regions with large-amplitude tides and complex coastlines.

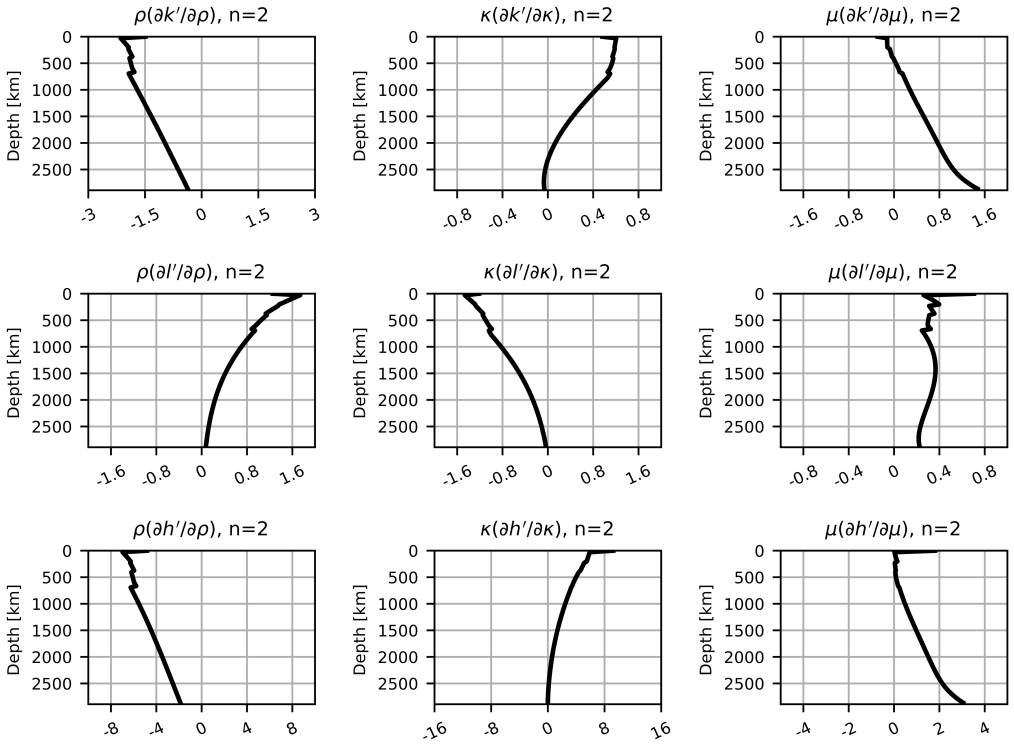

Figure S1. Partial derivatives of degree-2 load Love numbers (LLNs) derived from an oceanless variant of PREM with respect to density (left), the bulk modulus (center), and the shear modulus (right) through the crust and mantle of the Earth (cf. Martens et al., 2016b). The upper row of panels shows partial derivatives of the gravitational-potential LLN, k_2'; the middle row of panels shows partial derivatives of the horizontal-displacement LLN, l_2'; and the bottom row of panels shows partial derivatives for the vertical-displacement LLN, h_2'. The oceanless variant of PREM we have used is equivalent to that adopted by Guo et al. (2004) (see Table S1).

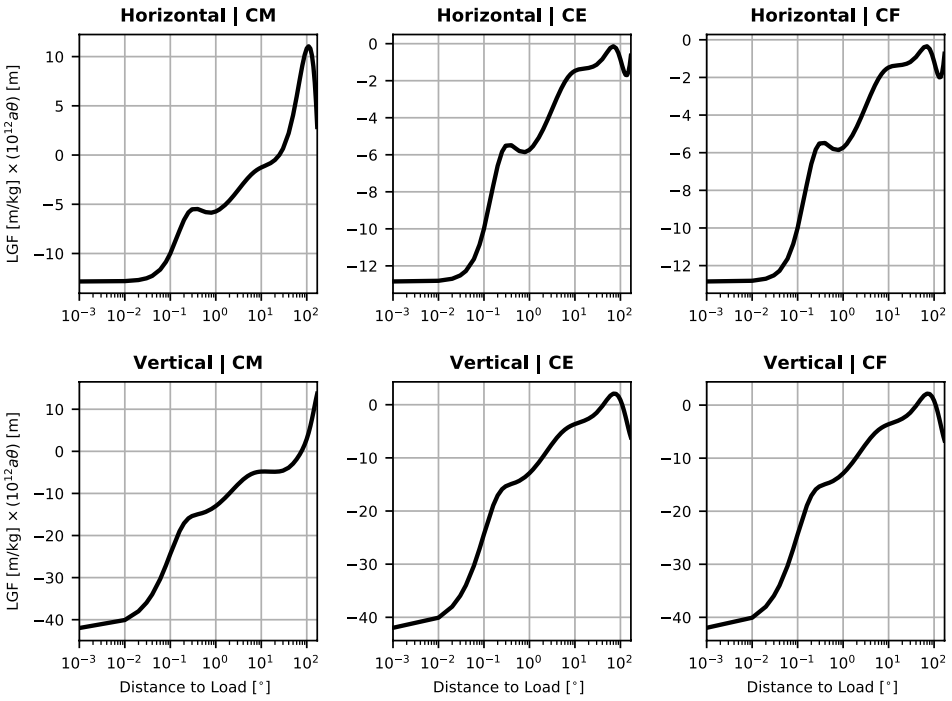

Figure S2. Displacement load Green's functions derived from an oceanless variant of PREM (see Table S1). The upper row of panels shows horizontal-displacement LGFs. The bottom row of panels shows vertical-displacement LGFs. From left to right, the LGFs correspond to the CM, CE, and CF reference frames.

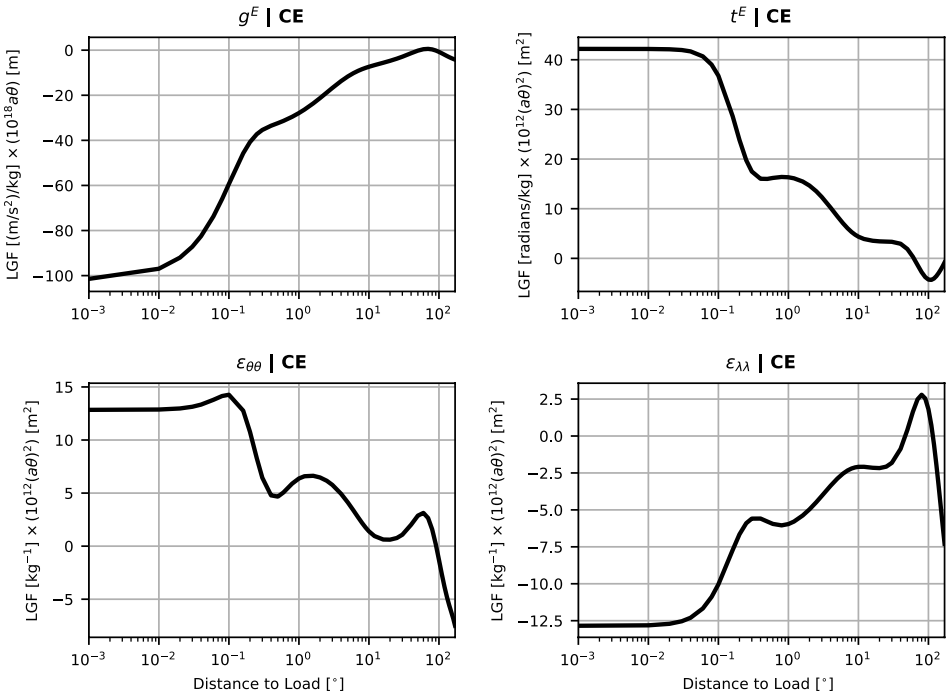

Figure S3. Gravity, tilt, and strain load Green's functions derived from an oceanless variant of PREM (see Table S1). For the gravity and tilt load Green's functions, only the elastic (i.e. indirect) contributions to the response are shown, although `LoadDef` computes both the elastic and Newtonian contributions. The two strain components are in the direction of the load ($\epsilon_{\theta\theta}$) and perpendicular to the load ($\epsilon_{\lambda\lambda}$).

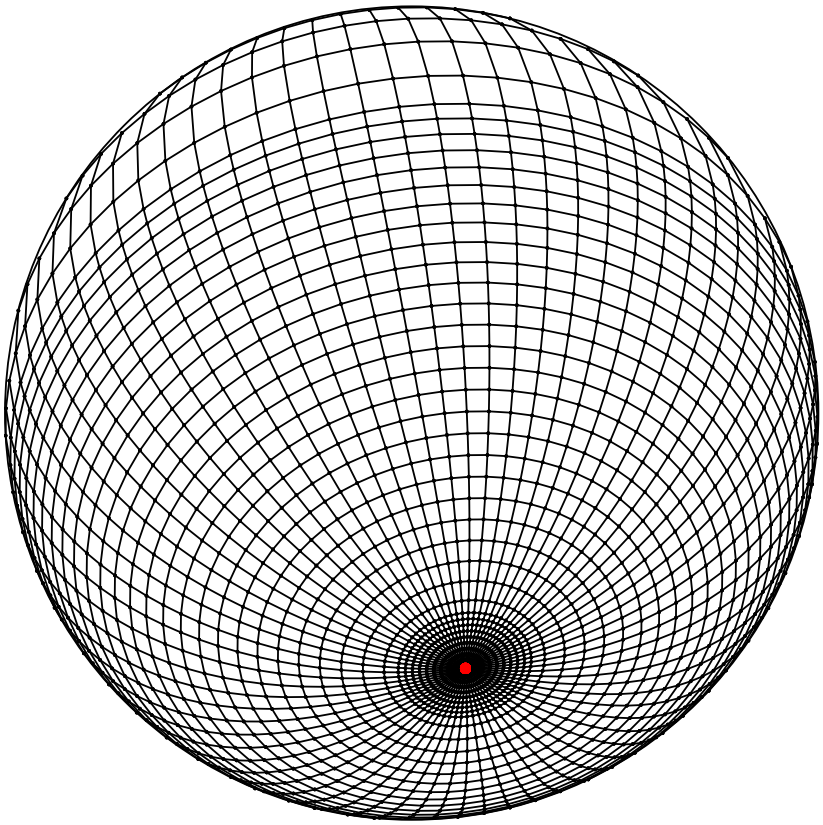

Figure S4. An example of the template grid used to convolve load Green's functions with a surface mass-load model to predict three-component surface displacements at a particular geographic location. For visualization purposes, the spatial resolution of the template grid shown here is lower than the default grid in `LoadDef`. The template grid is centered on the geographic location of the prediction point, or "station" (red dot). The spatial resolution of the grid is highest at the station location, and reduces with distance away from the station. Settings controlling the spatial resolution of the template grid may be adjusted using keyword arguments.

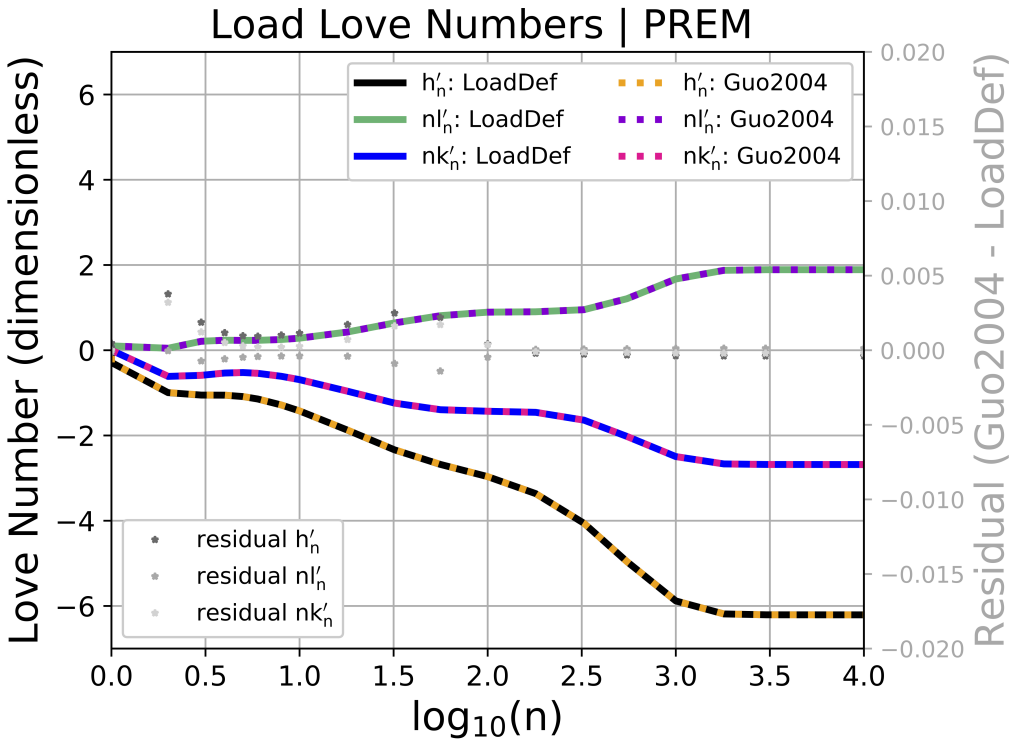

Figure S5. Benchmark comparison between a sampling of load Love numbers computed by `LoadDef` and the load Love numbers presented in Table 1 of Guo et al. (2004) (labeled `Guo2004` in the figure). Both sets of LLNs are derived from an oceanless variant of PREM (see Table S1). The `LoadDef` solutions are shown as solid lines and the `Guo2004` solutions are shown as dashed lines. The upper legend displays the color-coding for LLN type: h'_n (black solid and orange dashed), nl'_n (green solid and purple dashed), and nk'_n (blue solid and pink dashed). Note that the `LoadDef` and `Guo2004` LLNs overlap for each type of Love number, indicating good agreement between the two sources. Small residual differences between the LLNs are depicted by the grey dots (see lower legend). The second y-axis on the right-side provides the scale for the residual differences. The LLNs and the residual differences between the LLNs are dimensionless.

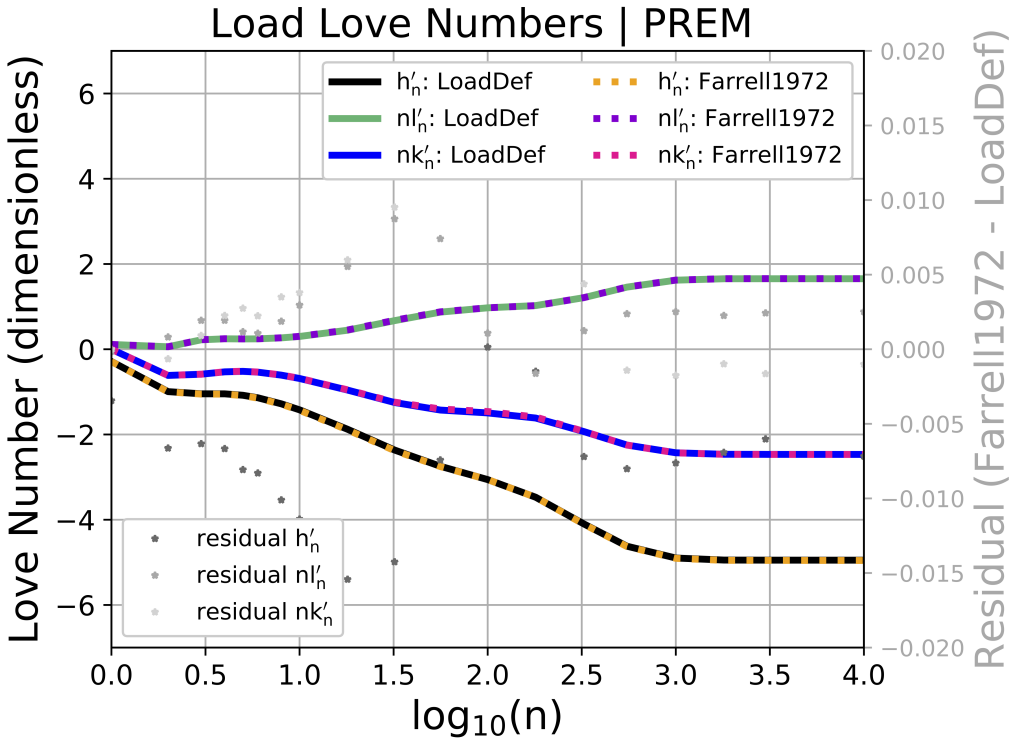

Figure S6. Benchmark comparison between a sampling of load Love numbers computed by `LoadDef` and the load Love numbers presented in Table A2 of Farrell (1972) (labeled `Farrell1972` in the figure). The solid lines depict the LLNs computed by `LoadDef` and the dashed lines depict the LLNs from `Farrell1972`. The upper legend displays the color-coding for LLN type: h'_n (black solid and orange dashed), nl'_n (green solid and purple dashed), and nk'_n (blue solid and pink dashed). Note that the `LoadDef` and `Farrell1972` LLNs overlap for each type of Love number, indicating good agreement between the two sources. Small residual differences between the LLNs are depicted by the grey dots (see lower legend). The second y-axis on the right-side provides the scale for the residual differences. Both sets of LLNs are derived from the Gutenberg-Bullen Earth Model A (GBA) (Alterman et al., 1961, Table 4). To best match the results of Farrell (1972), it was necessary to characterize the Earth model as a block-type model (i.e. no interpolation between material layers). We also assumed the shear-wave velocities of PREM for the inner core, since shear-wave velocities for the inner core are not included in the GBA model. Inner-core structure affects only the low-degree Love numbers. The residual differences exhibit significantly more scatter than the comparison with Guo et al. (2004) in Fig. S5, likely reflecting improvements in numerical computation over time as well as minor discrepancies in Earth model that arise with conversion to a block-type model and inclusion of an inner core.

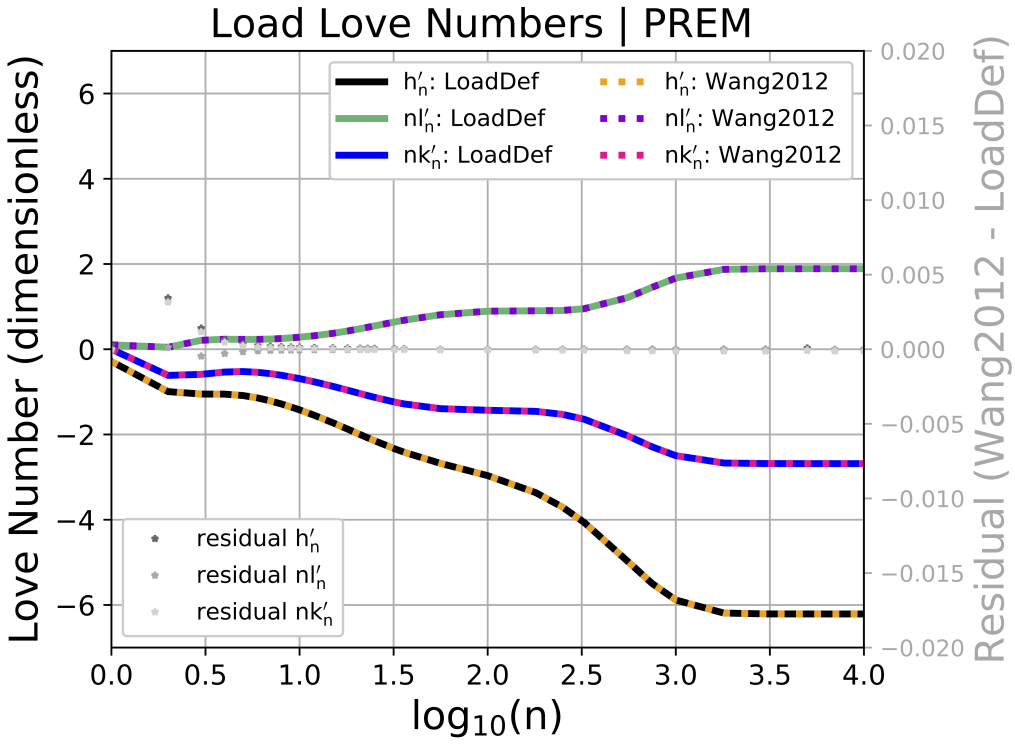

Figure S7. Benchmark comparison between a sampling of load Love numbers computed by `LoadDef` and the load Love numbers provided in the supplementary materials of Wang et al. (2012) (labeled `Wang2012` in the figure). The solid lines depict the LLNs computed by `LoadDef` and the dashed lines depict the LLNs from `Wang2012`. The upper legend displays the color-coding for LLN type: h'_n (black solid and orange dashed), nl'_n (green solid and purple dashed), and nk'_n (blue solid and pink dashed). Note that the `LoadDef` and `Wang2012` LLNs overlap for each type of Love number, indicating good agreement between the two sources. Small residual differences between the LLNs are depicted by the grey dots (see lower legend). The second y-axis on the right-side provides the scale for the residual differences. Both sets of LLNs are derived from an oceanless variant of PREM similar to Table S1, provided by H. Wang (personal communication).

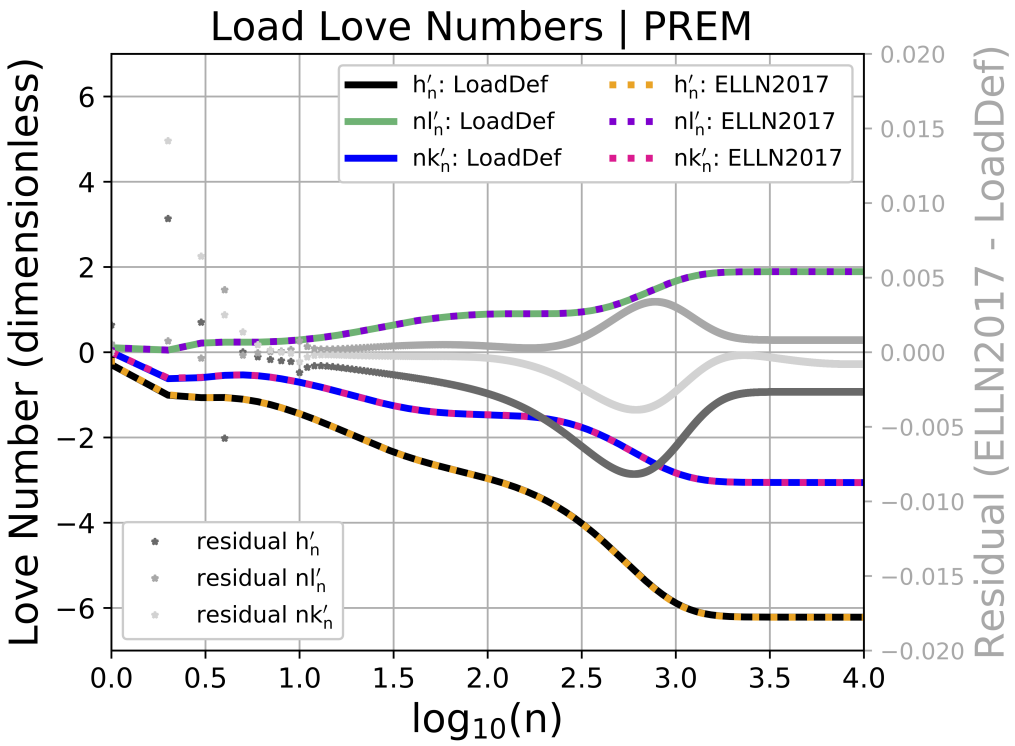

Figure S8. Benchmark comparison between LLNs computed by `LoadDef` and LLNs computed using the ELLN software package developed by Chen et al. (2017) (labeled `ELLN2017` in the figure). The solid lines depict the LLNs computed by `LoadDef` and the dashed lines depict the LLNs from `ELLN2017` (see upper legend). Note that the `LoadDef` and `ELLN2017` LLNs overlap for each type of Love number, indicating good agreement between the two sources. Small residual differences between the LLNs are depicted by the grey dots (see lower legend). The second y-axis on the right-side provides the scale for the residual differences. For the comparison, we used the example Earth models provided with `ELLN2017`: `EarthCore26.txt` and `EarthMantle56.txt`. We assumed isotropic, layered and compressible structure. `ELLN` further assumes a fully fluid core as well as constant elastic moduli within each layer. In addition, `ELLN` assumes constant gravity within each layer of the mantle region and constant density within each layer of the core region. We adapt the `ELLN2017` example Earth models for input into `LoadDef` by simulating a block-type model (i.e. no variation in elastic moduli or density within each layer). We do so by inserting extra entries into the Earth model a short distance (100 m) above the base of each original layer. The new entries inherit the material properties of the top of each original layer. Although the Earth-model modification is not a perfect reproduction of the `ELLN2017` model and methods, the modification allows for an improved comparison over the original model. Furthermore, since `LoadDef` requires a solid inner core to begin the integration, we replace the deepest layer in `EarthCore26.txt` with the deepest layer of PREM; model differences in the inner-core region affect only the low-degree Love numbers. The smooth residual differences (grey dots) between the LLNs, most pronounced between about n=100 and n=1000, are likely related to the small differences in Earth-model characterization and treatment described above. The scatter at lower degrees may represent, at least in part, minor differences in the equations of motion: `LoadDef` retains the inertial terms in the equations of motion, whereas `ELLN2017` adopts a static formulation. Inclusion of the inertial terms in the equations of motion primarily affects the fluid core region (e.g. Longman, 1963; Pekeris & Accad, 1972; Chinnery, 1975; Smylie, 2013). Both LLN curves are individually smooth, indicating minimal numerical instabilities in both cases.

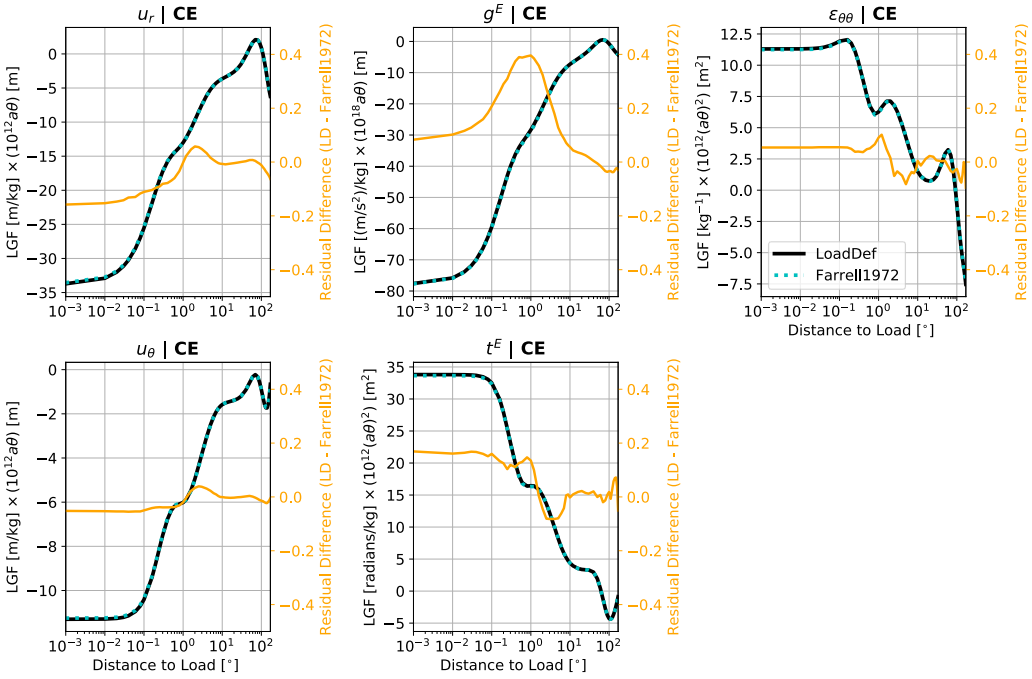

Figure S9. Benchmark comparison between load Green's functions computed by `LoadDef` (solid black lines) and those computed by Farrell (1972) (dashed blue lines) for the Gutenberg-Bullen A Earth model (see Table 4 of Alterman et al. (1961)). To remain consistent with Farrell (1972) (referred to as `Farrell1972` in the figure), material properties are assumed constant within each layer. The panels show vertical displacement (u_r), horizontal displacement (u_θ), elastic gravity (g^E), elastic tilt (t^E), and strain in the direction of the load ($\epsilon_{\theta\theta}$). All responses are shown with respect to the CE reference frame. Note that the `LoadDef` and `Farrell1972` curves overlap in each panel, indicating good agreement between the two sets of results. To better decipher the minor discrepancies between the `LoadDef` and `Farrell1972` Green's functions, we compute the residual differences between the two curves. The residual differences are depicted by the orange lines in each panel. Note the change in scale for the second y-axis on the right-side of each panel, which corresponds to the residual differences. Units for the residuals are the same as for the Green's functions. Note that the scale for the residual differences differs from the comparison with Guo et al. (2004) in the main text (Fig. 2). The residuals between `LoadDef` and `Guo2004` are significantly smaller, likely owing to improvements in numerical computation over time and fewer discrepancies between input Earth models (see also Fig. S6).

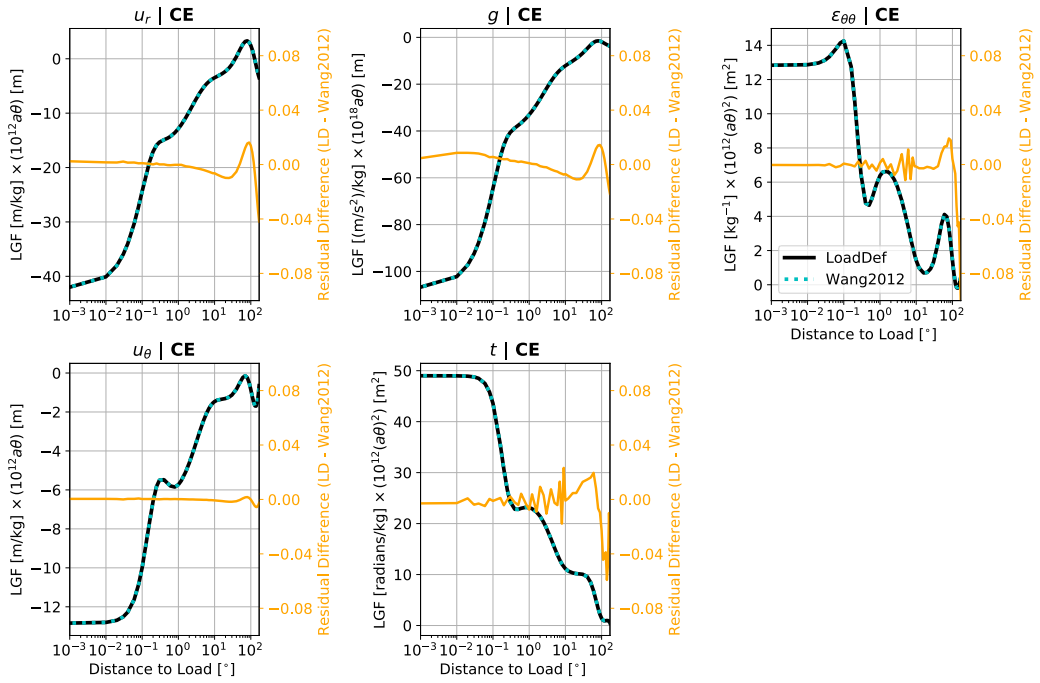

Figure S10. Benchmark comparison between load Green's functions computed by `LoadDef` (solid black lines) and those computed by Wang et al. (2012) (dashed blue lines) for an oceanless variant of PREM; see supplementary files in Wang et al. (2012). We refer to the LGFs from Wang et al. (2012) as `Wang2012` in the figure. The panels show vertical displacement (u_r), horizontal displacement (u_θ), gravity (g), tilt (t), and strain in the direction of the load ($\epsilon_{\theta\theta}$). Gravity and tilt include both the elastic (indirect) and Newtonian (direct) contributions to the response. Degree-0 load Love numbers have been excluded from the summations for the purpose of mass conservation (Wang et al., 2012). All responses are shown with respect to the CE reference frame. Note that the `LoadDef` and `Wang2012` curves overlap in each panel, indicating good agreement between the two sets of results. To better decipher the minor discrepancies between the `LoadDef` and `Wang2012` Green's functions, we compute the residual differences between the two curves. The residual differences are depicted by the orange lines in each panel. Note the change in scale for the second y-axis on the right-side of each panel, which corresponds to the residual differences. Units for the residuals are the same as for the Green's functions. Note that the scale for the residual differences is equivalent to the comparison with Guo et al. (2004) in the main text (Fig. 2), but differs from the comparison with `Farrell1972` in Fig. S9.

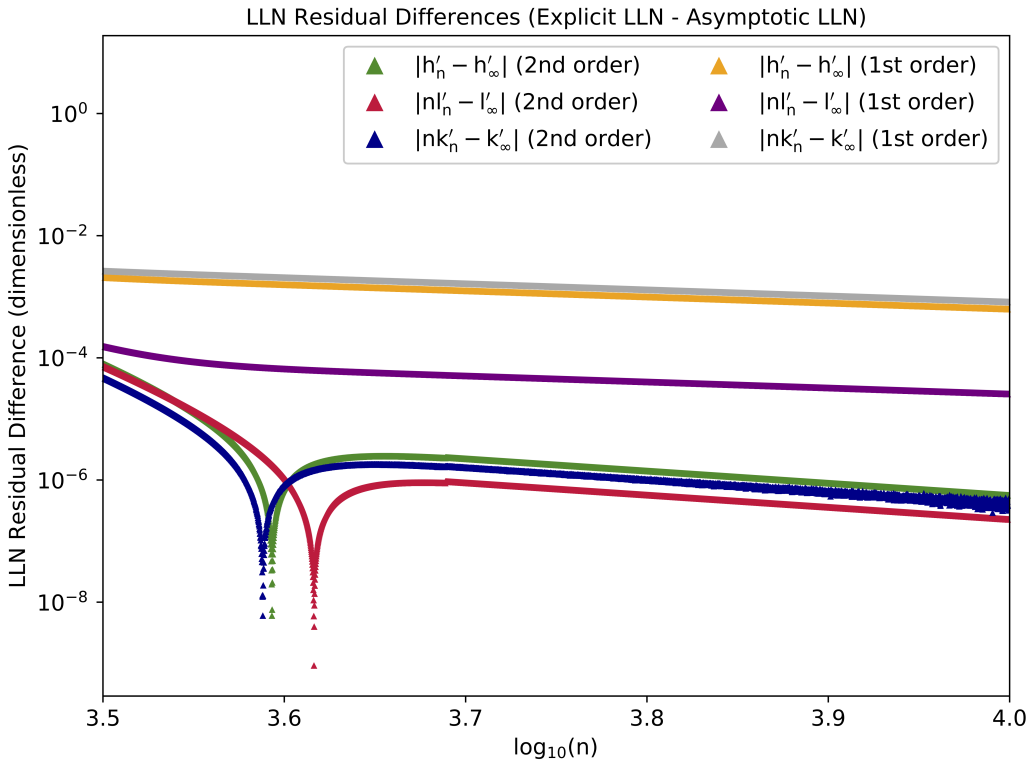

Figure S11. Comparison of first- and second-order asymptotic expansions of the load Love numbers at high n with LLNs computed explicitly within `LoadDef`. The curves represent the absolute value of the residual differences (on a logarithmic base-10 scale) between the LLNs computed explicitly in `LoadDef` and the asymptotic LLNs of either first- or second-order (see legend). Although the influence of the second-order term in the expansion diminishes with increasing spherical-harmonic degree, the second-order asymptotic load Love numbers converge to the true load Love numbers faster than the first-order asymptotic solutions. The log-scale also illuminates a consistent pattern that the displacement load Love numbers (h' and l') exhibit significantly greater stability than the gravity load Love numbers (k'). The gravity LLNs are used in the computation of the gravity and tilt LGFs, but only the displacement LLNs are used in the computation of load-induced surface displacements. The perturbations to the k'_n due to numerical instabilities are small (on the order of 10^{-7} at n=10,000), and much smaller than the differences between the first- and second-order asymptotic solutions. The residual differences between the explicitly computed LLNs and the second-order asymptotic solutions cross zero at approximately $n = 4000$, as evidenced by the figure.

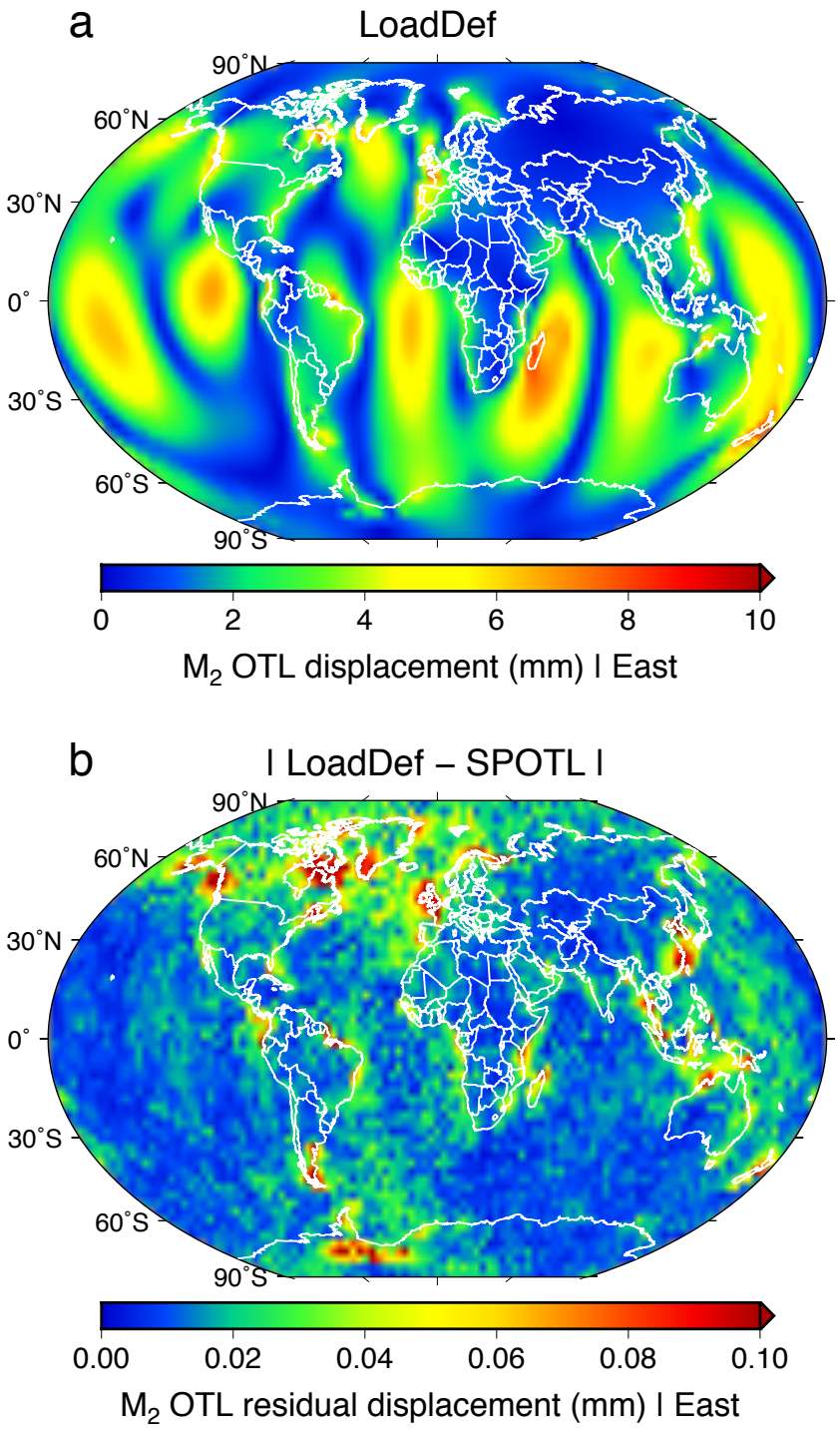

Figure S12. (a) Surface displacements (east component) caused by M_2 ocean tidal loading as modeled by `LoadDef`. Only the amplitude of the response is shown, here with respect to the CE reference frame. We have used the EOT11a ocean-tide model and the GBA Earth model as input to the convolution. `SPOTL` results are indistinguishable from `LoadDef` results at this amplitude scale; thus, the `SPOTL` results are not shown. (b) Vector differences between OTL-generated surface displacements computed by `LoadDef` and `SPOTL`. The GBA and EOT11a models were used for both computations, and the differences were computed using the in-phase and quadrature components. Note the change in amplitude scale between the absolute response in panel (a) and the residuals in panel (b). Only small differences between the modeling results exist, with the largest differences manifesting in regions with large tidal amplitudes and complex coastlines.

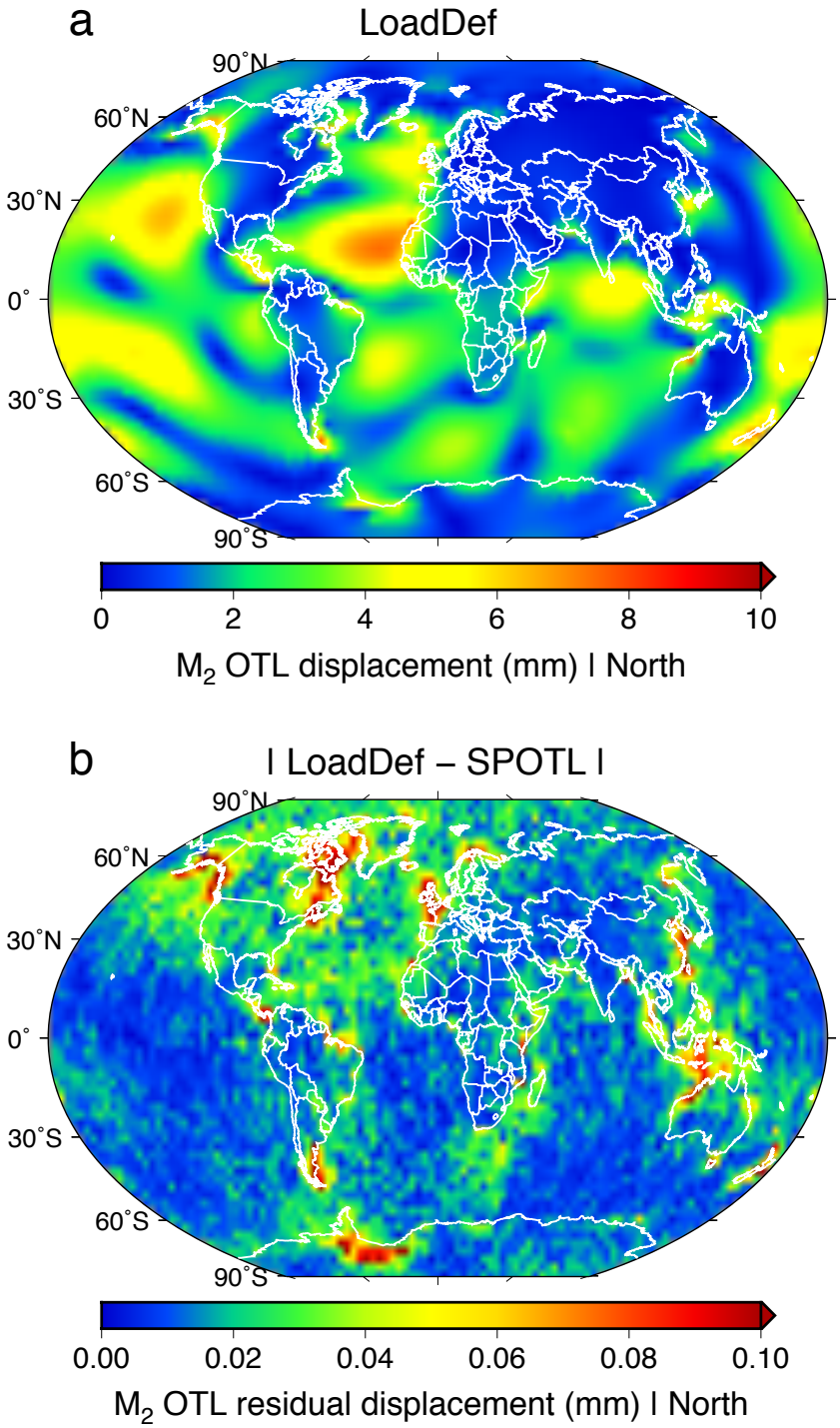

Figure S13. Same as Fig. S12, but for the north component of displacement. Figure 4 in the main text shows the vertical component of displacement.

References

Abramowitz, M., & Stegun, I. A. (1964). *Handbook of mathematical functions: With formulas, graphs, and mathematical tables*. Courier Corporation, Dover Publications, New York.

Agnew, D. C. (1997). NLOADF: A program for computing ocean-tide loading. *J. Geophys. Res.*, *102*(B3), 5109–5110.

Agnew, D. C. (2013). SPOTL: Some programs for ocean-tide loading. *Scripps Institute of Oceanography Technical Report*. Retrieved from `https://igppweb.ucsd.edu/ agnew/Spotl/spotlman.pdf`

Alterman, Z., Jarosch, H., & Pekeris, C. (1959). Oscillations of the Earth. *Proc. R. Soc. London, Ser. A*, *252*(1268), 80–95.

Alterman, Z., Jarosch, H., & Pekeris, C. (1961). Propagation of rayleigh waves in the earth. *Geophys. J. Int.*, *4*(Issue Supplement_1), 219–241.

Chen, J., Pan, E., & Bevis, M. (2017). Accurate computation of the elastic load Love numbers to high spectral degree for a finely layered, transversely isotropic and self-gravitating Earth. *Geophys. J. Int.*, *212*(2), 827–838.

Chinnery, M. A. (1975). The static deformation of an earth with a fluid core: a physical approach. *Geophys. J. R. Astron. Soc.*, *42*(2), 461–475.

Dziewonski, A. M., & Anderson, D. L. (1981). Preliminary reference Earth model. *Phys. Earth Planet. Inter.*, *25*(4), 297–356. doi: 10.1016/0031-9201(81)90046-7

Farrell, W. (1972). Deformation of the Earth by surface loads. *Rev. Geophys.*, *10*(3), 761–797.

Guo, J., Li, Y., Huang, Y., Deng, H., Xu, S., & Ning, J. (2004). Green's function of the deformation of the Earth as a result of atmospheric loading. *Geophys. J. Int.*, *159*(1), 53–68. doi: 10.1111/j.1365-246X.2004.02410.x

Longman, I. (1963). A Green's function for determining the deformation of the Earth under surface mass loads: 2. Computations and numerical results. *J. Geophys. Res.*, *68*(2), 485–496. doi: 10.1029/JZ068i002p00485

Martens, H. R., Rivera, L., Simons, M., & Ito, T. (2016b). The sensitivity of surface mass loading displacement response to perturbations in the elastic structure of the crust and mantle. *J. Geophys. Res. Solid Earth*, *121*. doi: 10.1002/2015JB012456

Na, S.-H., & Baek, J. (2011). Computation of the load Love number and the load Green's function for an elastic and spherically symmetric earth. *J. Korean Phys. Soc.*, *58*(5), 1195–1205.

Pekeris, C. L., & Accad, Y. (1972). Dynamics of the liquid core of the Earth. *Philos. Trans. R. Soc. London, Ser. A*, *273*(1233), 237–260.

Smylie, D. (2013). *Earth Dynamics: Deformations and Oscillations of the Rotating Earth*. Cambridge University Press.

Wang, H., Xiang, L., Jia, L., Jiang, L., Wang, Z., Hu, B., & Gao, P. (2012). Load Love numbers and Green's functions for elastic Earth models PREM, iasp91, ak135, and modified models with refined crustal structure from Crust 2.0. *Computers & Geosciences*, *49*, 190–199. doi: 10.1016/j.cageo.2012.06.022